Available online at www.sciencedirect.com
ScienceDirect
Journal of Molecular Catalysis A: Chemical 273 (2007) 198–210
JOURNAL OF MOLECULAR CATALYSIS A: CHEMICAL
www.elsevier.com/locate/molcata

Synthesis and characterization of mordenites encapsulated titania nanoparticles: Photocatalytic degradation of *meta*-chlorophenol

Tarek Mohamed Salama [a], Ibraheem Othman Ali [a], Mohamed Mokhtar Mohamed [b,*]

[a] *Faculty of Science, Chemistry Department, Al-Azhar University, Nasr City, Cairo, Egypt*
[b] *Faculty of Science, Chemistry Department, Benha University, Benha, Egypt*

Received 14 January 2007; accepted 27 March 2007
Available online 31 March 2007

Abstract

Titanium-mordenites catalysts prepared by impregnation (TiM_{imp}), solid-solid interaction (TiM_{ss}) and in situ incorporation during synthesis (TiM_{in}); using *ortho*-phenylenediamine as a new templating agent under hydrothermal conditions ($TiCl_4$, 160 °C, 6 days), were thoroughly characterized by TG/DTA, N_2 adsorption, XRD, FTIR, UV–vis and pyridine-FTIR. They were tested; in comparison with TiO_2 Degussa, for degradation of *meta*-chlorophenol (MCP) in the presence of UV-light irradiation. It was possible to correlate the results obtained for MCP degradation over various catalysts with their structural and acidic properties. The photocatalytic degradation of MCP has been modeled to Langmuir-Hinshelwood rate law. TiM_{ss} showed the highest degradation rate (0.060 min^{-1}) followed by those of TiM_{imp} (0.050 min^{-1}), TiM_{in} (0.025 min^{-1}) and TiO_2-Degussa (0.018 min^{-1}), respectively. The marked higher rate observed for the former catalyst was due to the larger pore radius (29 Å), acidity and the extra-framework TiO_2 anatase species (of absorption at 340 nm). Very strong emphasize to the state of titania within the three samples (TiM) was demonstrated and most importantly Si—O—Ti linkages (950–940 cm^{-1}) were observed and correlated with photoactivities of all samples. Degradation products of MCP, including both aromatic and aliphatic intermediates, were monitored by HPLC. Chloride ions, on the other hand, were followed up during the degradation processes. Formic acid (formate) was identified as a final intermediate in the solution before it further mineralized to CO_2. Reasonable degradation pathway for MCP molecule is proposed on the basis of structural identification of several by-products.

Keywords: Mordenite; Synthesis; Ti-incorporation; Characterization; Photocatalytic degradation

1. Introduction

Mordenite is an industrially important zeolite used as solid catalyst for conversion of hydrocarbons and is recently being considered for applications as host of semiconductor materials, chemical sensors and non-linear optical materials [1–4]. Therefore, there are a lot of articles and patents concerning the synthesis of mordenite zeolite crystals in the absence or presence of organics such as piperazine and polyglycol [5–8]. Isomorphous substitution of a metal ion into the framework, on the other hand, of mordenite is very effective in exhibiting spectacular catalytic properties based on the acidity of the bifunctional metal ion–zeolite system [9–10].

A comprehensive study of the synthesis of mordenite using a new template (*ortho*-phenylenediamine [OPDA]) was carried out in our labs in a way of synthesizing mordenite zeolite with varying pore geometry and high Si/Al ratio [11].

Titanium atoms incorporated into the zeolite framework serve as catalytic sites thus; the content of framework titanium in a zeolite has presented higher activity in performing some catalytic reactions [12–15]. TiO_2 in mixed phase materials are the best photocatalyst reported so far [16]. However, poor adsorption and low surface area properties lead to great limitations in exploiting the photocatalyst to the best of its photoefficiency. Supported TiO_2 is commonly reported to be less photoactive due to the interaction of TiO_2 with the support during the thermal treatments [17]. Several attempts have been made to improve the photoefficiency of titania by adding adsorbents like silica, alumina, zeolites, clays, and active carbon [18–23]. Zeolite based photocatalysis is increasingly attracting many researchers and not yet well explored and the work reported so far involved the

* Corresponding author. Present address: Faculty of Applied Science, Umm Al-Qura University, Makka, P.O. Box, 6503 Unit 71, Saudi Arabia.
Tel.: +966 500969808.
E-mail address: mohmok2000@yahoo.com (M.M. Mohamed).

1381-1169/$ – see front matter © 2007 Elsevier B.V. All rights reserved.
doi:10.1016/j.molcata.2007.03.071

use of high TiO_2 loadings [24]. On the other hand, the higher dispersion state of Ti oxide species inside zeolite frameworks are prerequisites to effective photocatalytic reactions such as reduction of CO_2 by $H_2O$and NO decomposition into N_2 [25,26]. Nanoscale anatase materials are also reported to be highly active probably due to high surface areas rather than intrinsic improvement in reactivity [27,28].

In a way of designing an efficient local structure for hosting TiO_2 photocatalyst to control the activity, mordenite zeolite was synthesized and used as a support for TiO_2; that can be excited under UV-irradiation forming charge-transfer excited state thus involving an electron transfer from O_2^- to Ti^{4+} [29]. Accordingly, the preparation of Ti-mordenite by three different methods namely in situ incorporation during synthesis, impregnation and solid-solid interaction were carried out. These samples have been characterized by thermal analysis, X-ray diffraction, N_2 adsorption, FT-IR, UV–vis and pyridine-FT-IR techniques. The photocatalytic activity of the samples towards degradation of *meta*-chlorophenol was studied; using HPLC, together with revealing the performance of the catalysts, and the possible reaction mechanism.

2. Experimental

2.1. Materials

The materials used were: silicic acid powder, sodium hydroxide pellets (A.R. 98%), aluminum sulfate [Merck, $Al_2(SO_4)_3{\cdot}16H_2O$], *o*-phenylenediamine (Merck), acetyl acetone and titanium tetrachloride (BDH 99% $TiCl_4$) and commercial H_2SO_4.

2.1.1. Preparation of mordenite

The hydrogels of the following oxide molar compositions were prepared for the synthesis of mordenite zeolite.

$$3.12Na_2O : 0.16Al_2O_3 : 6.185SiO_2 : 0.185Q : 100H_2O$$

where Q is *o*-phenylenediamine (OPDA) template.

A known amount of NaOH was added to silicic acid/H_2O system while stirring, followed by heating at 80 °C until clear solution was obtained. The OPDA was dissolved in 10 ml of H_2O followed by heating at 50 °C for 20 min. Then, the solution of OPDA was added to that of sodium silicate while stirring for 15 min. The aluminum sulfate, on the other hand, was dissolved in calculated amount of H_2O with adding 0.05-ml concentrated H_2SO_4. To the latter solution, the combined solution of sodium silicate and OPDA was added followed by stirring for 30 min. The pH of the mixture was adjusted to 11 by using NaOH (0.1 M) and H_2SO_4 (0.1 M) solutions. Finally, the mixture was hydrothermally treated at 160 °C in an oil bath, using stainless steal autoclaves for 6 days. The autoclaves were removed at the prespecified time from the oil bath and were quenched immediately with cold water. The solid product was filtered and washed with distilled water until the pH of the filtrate dropped to 8. The products were dried at 110 °C for 10 h then calcined at 550 °C for 6 h in an air oven. This sample was referred to as M.

2.1.2. Preparation of Ti-mordenite (built-in)

The synthesis procedure is described in molar compositions as follows:

$$3.12Na_2O : 0.1Al_2O_3 : 0.062TiO_2 : 6.185SiO_2 : 0.185Q : 100H_2O$$

The calculated amounts of sodium hydroxide and silica were added to deionized water and stirred with heating at 80 °C until the silica was dissolved. Another clear solution of OPDA was prepared into which a calculated amount of $TiCl_4$ was added parallel with 2 ml of acetyl acetone followed by vigorous stirring at room temperature for 15 min. The aluminum sulfate, on the other hand, was dissolved in calculated amount of H_2O with adding 0.05-ml concentrated H_2SO_4. A simultaneous addition of the silicate solution was carried out into the complex (composed of OPDA containing $TiCl_4$ and aluminum sulphate) followed by stirring for 30 min till homogenization of the mixture was achieved. Then, the reaction mixture was transferred to a 300 ml stainless-steel autoclave and maintained in the oil bath at 180 °C, for the crystallization period of 10 days under autogeneous pressure. The Autoclave was removed from the oil bath and quenched under cold water for product identification. The solid product was filtered and washed with distilled water until the pH of the filtrate dropped to 8. The solid product was then dried at 120 °C for 10 h and calcined at 550 °C for 6 h. This sample was referred to as TiM_{in}.

2.1.3. Preparation of TiO_2 in mordenite by solid-solid interaction

This sample was prepared by the mechanical mixing of mordenite that synthesized in this work of $S_{BET} = 324\ m^2/g$ with TiO_2 sample. Mordenite was degassed at 300 °C for 3 h (under a reduced pressure of 10^{-5} Torr) prior to mechanically mixing with TiO_2 (prepared by hydrolysis of $TiCl_4$ using NH_4OH, washed with distilled water, heated at 110 and finally calcined at 550 °C) then left under stirring in a schlink tube overnight under a flowing nitrogen gas at a rate of 30 cm^3/min. The sample was evacuated in a conventional high vacuum manifold ($\sim 10^{-5}$ Torr) system while the temperature was slowly increased at a ramping rate of 0.33 °C/min till 300 °C at which the temperature was kept constant for 4 h. The prepared sample gave TiO_2 loading 6.5 on the bases of molar ratio. The sample was calcined at 550 °C, in air for 6 h. The obtained sample was referred to as TiM_{ss}.

2.1.4. Preparation of TiO_2 in mordenite by impregnation method

This sample was prepared by impregnation of mordenite that synthesized in this work. Na-mordenite was stirred with a solution of $TiCl_4$ to give TiO_2 loading of 6.5 on the bases of molar ratio. The sample was dehydrated in an oven 110 °C for 6 h at and was eventually calcined at 550 °C for 6 h. The obtained sample was referred to as TiM_{imp}. TiO_2 purchased from Degussa (P-25 having 85% anatase and 15% rutile of surface area 50 m^2/g) was used for comparison purposes.

2.2. Characterization techniques

The X-ray diffraction patterns of various zeolite samples were measured by using a Philips diffractometer (type PW 3710) equipped with Cu Kα radiation. The samples were measured in the 2θ range of 10–50° at 30 kV and 10 mA with a scanning speed of $2\theta = 2.5°\ min^{-1}$. The crystal sizes of the prepared materials were determined using the Scherrer equation. The instrumental line broadening was measured using a LaB6 standard. The crystallinity of the modified samples was calculated using the ratio of the sum of the areas of the most intense peaks for the prepared samples ($2\theta = 16.8$, 19.6, 22.2, 28.2 and 32.3 Å) to that of the same peaks of as-synthesized Na-mordenite; of this work, and multiplying by 100. Rietveld method, which permits the reproduction of the whole diffractogram through the optimization of both structural (peak position and intensity) and non-structural (peak shape) data is used to evaluate the determination of cell parameters and volume increase due to insertion of guest ions in the zeolite structure.

In situ FT-IR spectra of the samples were recorded with JASCO single beam FT-IR 5300 spectrometer with 50 co-added scans at $2\ cm^{-1}$ resolution. The sample was pressed into a self-supporting wafer and mounted in a quartz infrared cell with CaF_2 windows that connected to vacuum manifold (10^{-5} Torr) constructed of Pyrex glass with a dead volume of 301 cm^3. The infrared cell was equipped with an electric furnace and the sample temperature was adjusted by using the temperature controller connected to a thermocouple made of nickel chrome. The IR sample was prepared by pressing the catalyst powder ground in an agate mortar to a wafer of ca. 30 mg cm^2 and then outgassing at 300 °C for 3 h before exposure to reactant gases. IR measurements were all carried out at room temperature. All of the spectra presented were obtained by subtraction of the corresponding background reference.

The IR spectral changes of pyridine adsorption were measured in the 1700–1400 cm^{-1} region. Pyridine (10 Torr) was admitted into the cell and equilibrated with the sample for 30 min. Excess pyridine was then pumped out before recording the spectra: pyridine was pumped out at 25 and 100 °C each time.

UV–vis diffuse reflectance spectra of the samples were measured using a JASCO V-570 unit, serial no. (29635), at scanning speed 4000 nm/mm and a bandwidth 2 nm. The samples were measured in the wavelength range from 200 to 500 nm. The samples were prepared as self-supporting wafers and were recorded at room temperature.

TG and DTA thermograms were performed for uncalcined samples (10 mg) using Model 50 Shimadzu units in the range of 25–1000 °C with a temperature rise of 10 °C/min. Dry nitrogen was used as a purge gas at a rate of 30 ml/min.

The nitrogen adsorption isotherms were measured at −196 °C using a conventional volumetric apparatus. The specific surface area was obtained using the BET method. The micropore volume and the external surface area were obtained from the *t*-plot method.

Experiments in the darkness were performed to determine the amounts of MCP adsorbed on different TiO_2-mordeites. The adsorption capacity of *m*-chlorophenol (MCP) was measured with adjusting the pH at 6.5. In 250 ml of MCP solution at initial concentration of 5×10^{-3} M, 0.1 g of samples were added and then agitated in the darkness for 30 min. The suspensions were centrifuged to remove TiO_2 particles and the retained concentration of MCP, C was determined. The amount of MCP adsorbed onto the TiO_2-zeolites was determined by the difference between the initial and the retained concentration of MCP divided by the initial concentration of MCP:

$$\text{uptake}\ \% = \frac{C_o - C}{C_o} \quad (1)$$

The photoreactivity experiments were carried out in a cylindrical Pyrex glass reactor containing 0.10 g of catalyst and 250 ml of aqueous solution of *meta*-chlorophenol (MCP). The concentration of the organic compound was 5×10^{-3} M. A 125 W medium pressure Hg lamp (312 nm) immersed within the photoreactor was used and the mean value of the incident radiation power, determined using an UV (Digital UVX 36) was 13.5 mW cm^2. The Products were analyzed by HPLC using Dionex p580 pump equipped with a Dionex column DX-120 by means of ion chromatography Dionex-pac attached with AS14 column. Chloride ions were determined through using LiChrospher RP-18 column (4 mm × 125 mm). Acetonitrile was used as eluent at 1 ml/min.

3. Results and discussion

3.1. Thermal analyses

TG and DTA thermograms of uncalcined M and TiM_{in} samples are shown in Fig. 1; in the temperature range from 25 to 1000 °C. TG analyses indicate that the total weight loss of TiM_{in} (17.5%) is exceeding that of M (14%). The low temperature weight losses are associated with the removal of water while the high temperature ones are due to the decomposition of the template OPDA. Correspondingly, two endothermic peaks at 128 and 153 °C are observed in the DTA curves for M and TiM_{in}, respectively. This indicates that the interaction between water molecules and titano-aluminosilicate is stronger than that with aluminosilicate structure. This could give a hint about the microporosity of the former comparatively. Varying the decomposition temperatures of the template for M (322 and 537 °C) and TiM_{in} (402, 496 and 552 °C) samples indicate that the interaction of template has different strengths within the two samples. The weight loss expressing OPDA decomposition, on the bases of sharing four molecules per unit cell (4.75%), indicates lower amount in M (3.71%) and higher amount in TiM_{in} (7.86%). In addition, exceeding the endothermic maxima appeared at 402 and 552 °C in TiM_{in} than those seen in M (322 and 537 °C) verified the strong association of the template within titanoaluminosilicate structure comparatively. This means that OPDA molecules will find some restrictions during decomposition in the narrow pores present in TiM_{in} (552 °C) than that in M (537 °C). This was in agreement with the observed decrease in weight loss of TiM_{in} when compared with that of M in the temperature range 510–570 °C. However, the observed increase

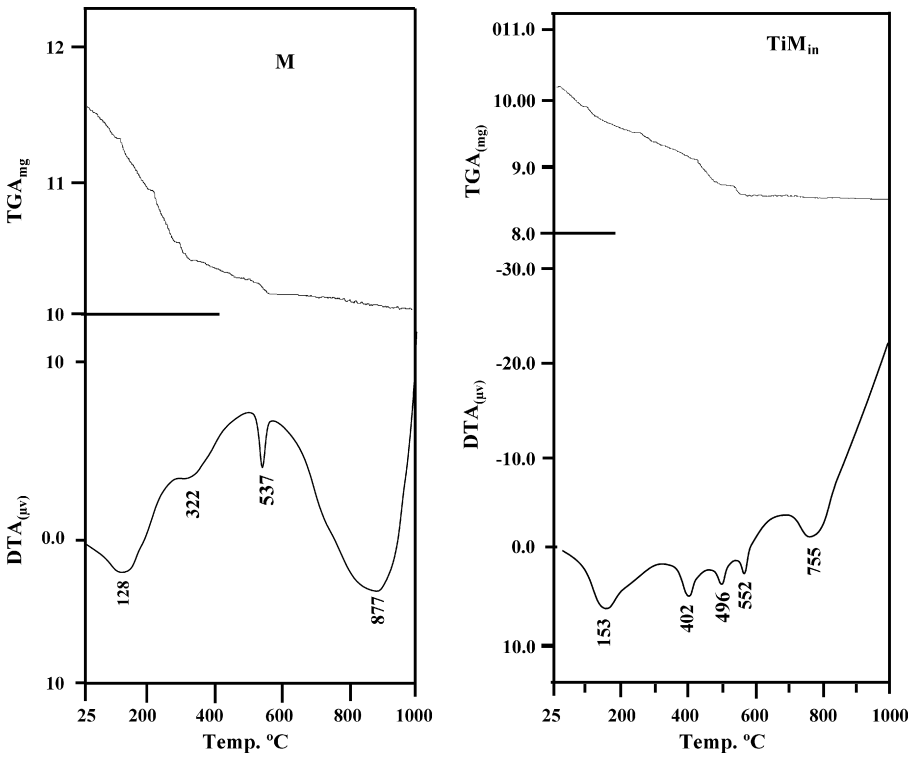

Fig. 1. TGA and DTA curves of uncalcined mordenite and Ti-mordenite samples synthesized by *ortho*-phenylenediamine template.

in weight loss of TiM_{in} in the 300–510 °C range than that of M implies also the presence of wider pores in TiM_{in} indicating that it acquires micro-mesoporous structure. This was in harmony with the total pore volume results that showed an enhancement in TiM_{in} than that in M as a result of Ti incorporation. Ti incorporation in M was responsible for the earlier appearance of the endothermic peak at 755 that originally seen at 877 °C in M, confirming the lower thermal stability of the former comparatively.

3.2. X-ray diffractograms

Fig. 2 shows the XRD patterns of various Ti/mordenites synthesized by the three methods, in comparison with that of the parent mordenite synthesized in this work. The former patterns showed quite similar diffraction lines to that of the latter reflecting that they all have mordenite structure. However, minor variations were revealed, for example, TiM_{in} indicates small lines due to titanium-silicate; at $2\theta = 20.08$, 26.31, 28.40 and 30.44 Å [30], where TiM_{imp} and TiM_{ss} samples exhibit TiO_2 anatase lines at $2\theta = 37.70$, 38.45 and 47.87 Å in addition to non-exposed lines of same species in the range of $2\theta = 25$–28° due to exceeding the intensities of mordenite lines in this range rather than a decrease. No peaks for crystalline titania in TiM_{in} can be identified indicating probably the well incorporation of titania particles. Of particular interest, a shift into higher values of d for M was perceived in TiM_{in} exceeding TiM_{imp} and TiM_{ss} samples signifying the well incorporation of Ti in the framework of the former. The TiM_{in} pattern shows a partial loss in crystallinity with respect to the M sample where TiM_{imp} and TiM_{ss} samples show a marked decrease.

The lattice parameters (a, b, c) and unit cell volume (V) of Ti-mordenites are summarized in Table 1. Upon comparison, the unit cell parameters and volume of the TiM_{in} sample revealed an enhancement when compared with those of TiM_{imp} and TiM_{ss}, advocating the successful incorporation of Ti into the framework of mordenite in TiM_{in} replacing Si atoms that owned lower bond distances with oxygen (0.160 nm) than those of Ti–O (0.182 nm). Accommodating small titania particles in the micropores caused an expansion in unit cells and volume

Table 1
Effect of different preparation methods of Ti-mordenites on crystallites size, crystallinity percentages and unit cell parameters

Sample	Crystallite size D (nm)	Cell parameters (Å)			Cell volume V (Å)^3	Crystallinity (%)
		a	b	c		
Mordenite	48.40	18.129	20.413	7.387	2733.69	100
TiM_{in}	51.63	18.162	20.604	7.530	2817.77	86
TiM_{ss}	44.02	17.922	20.466	7.528	2761.10	62
TiM_{imp}	49.48	18.029	20.009	7.761	2799.92	53

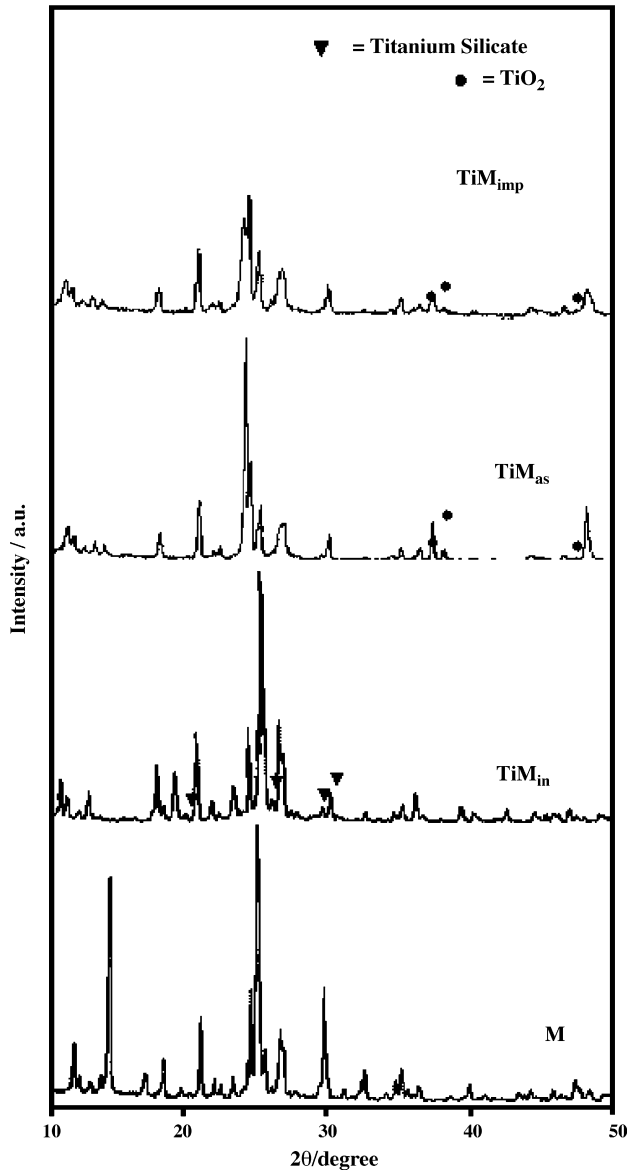

Fig. 2. X-ray diffraction patterns of mordenite and Ti-mordenites prepared by different methods.

for TiM_{in} and exceeded those of post-synthesis ones (TiM_{ss} and TiM_{imp}). One can notice that the strong interaction of $TiCl_4$ with M in TiM_{imp} was higher than that of TiO_2 with M in TiM_{ss} in the sense of decreasing the crystallinity of TiO_2 species in the former comparatively.

3.3. Texture assessment

The results of N_2-adsorption data obtained for all samples including the specific surface area, S_{BET}; total pore volume, V_p; average pore radius, r^-; micro and mesopores volumes and surfaces V_p^{μ}, V_p^{wid}, S^{μ} and S^{wid} are collected in Table 2. Inspecting this Table, an increase in S_{BET} and V_p is produced for TiM_{in} and TiM_{imp} samples when compared with that of the parent M. However, the TiM_{ss} sample indicates a decrease in S_{BET} (20%), V_p does not, and an increase in r^-, that was the largest value among all samples (29 Å, Table 2). Accommodation of small titania particles in the micropores of M in TiM_{ss} could be responsible for the devoted expansion of the pore radius. The external surface area S^{ext} of TiM_{in} (58 m^2/g), calculated from the slope of the V_{l-t} curve, is lower than that of M (66 m^2/g), confirming that TiM_{in} preserve higher microporous texturing. This microporsity was also emphasized by the percentage microporsity ($V_p^{\mu}/V_p \times 100$) that reached 85% (Table 2). Thus, one can attribute the small increase in S_{BET} of this sample (9.4%) when compared with M to titaniumsilicate species that has been emphasized by XRD investigations.

The sample TiM_{ss} possessed the lowest S_{BET} among all samples. This agrees with the greater r^- value of the sample. The high value of V_p^{wid} for TiM_{ss} also confirms the evolution of mesoporosity. Thus, the texture of sample TiM_{ss} appears more open than rest of the samples (wide), as TiM_{ss} possesses the highest r^- value, and also deep as that of M (equal V_p values).

On the other hand, the TiM_{imp} sample presented the highest S_{BET} (514 m^2/g) as the micropores are characterized by a high surface area. The microporosity of the TiM_{imp} sample is additionally confirmed from the percentage microporsity and reached 86% ($V_p^{\mu}/V_p \times 100$) exceeding rest of the samples (Table 2). This sample as is depicted from its V_{l-t} plot (not shown) indicates pore narrowing character; that was confirmed from the decreased value of r^-, resulted from blocking of some pores, the implication is that some pore narrowing has taken place in wide pores during calcination process giving that compensation effect. Growth of titania nanophase was clearly revealed on TiM_{imp} and TiM_{ss} samples when compared with TiM_{in}, as confirmed previously by XRD investigations.

3.4. IR spectra of various samples

The FT-IR spectra of Ti-mordenites and M samples are shown in Fig. 3. The IR spectrum of M shows bands at 1220, 1070, 791, 620, 563 and 455 cm^{-1}, which are assigned to different vibra-

Table 2
Some Surface characteristics of mordenite and TiO_2 loading by different preparation methods, heating at 300 °C under a reduced pressure of 10^{-5} Torr

Sample	S_{BET} (m^2/g)	S_t (m^2/g)	V_p^{total} (cm^3/g)	r^- (Å)	S^{μ} (m^2/g)	S^{ext} (m^2/g)	S^{wid} (m^2/g)	V_p^{μ} (cm^3/g)	V_p^{wid} (cm^3/g)	Microporosity (%)
Mor.	351	286	0.316	23	286	66	30	0.257	0.05892	81
TiM_{in}	384	371	0.347	23	327	58	26	0.295	0.05198	85
TiM_{ss}	280	262	0.319	29	226	54	31	0.258	0.06123	81
TiM_{imp}	514	442	0.418	20	440	74	30	0.358	0.05983	86

S_{BET}: total surface area determined using BET equation, S_t: specific surface areas determined from V_{l-t} plots of different adsorbents. S^{wid}: wide pore surface area, S^{μ} : micropores surface area, V_p^{wid}: the volume adsorbed in wide porous, V_p^{μ}: micropore volume , r^- (Å): average pore radius, V_p^t: the total pore volume at $p/p^0 = 0.95$, S_{ext}^t: external surface area of microporous.

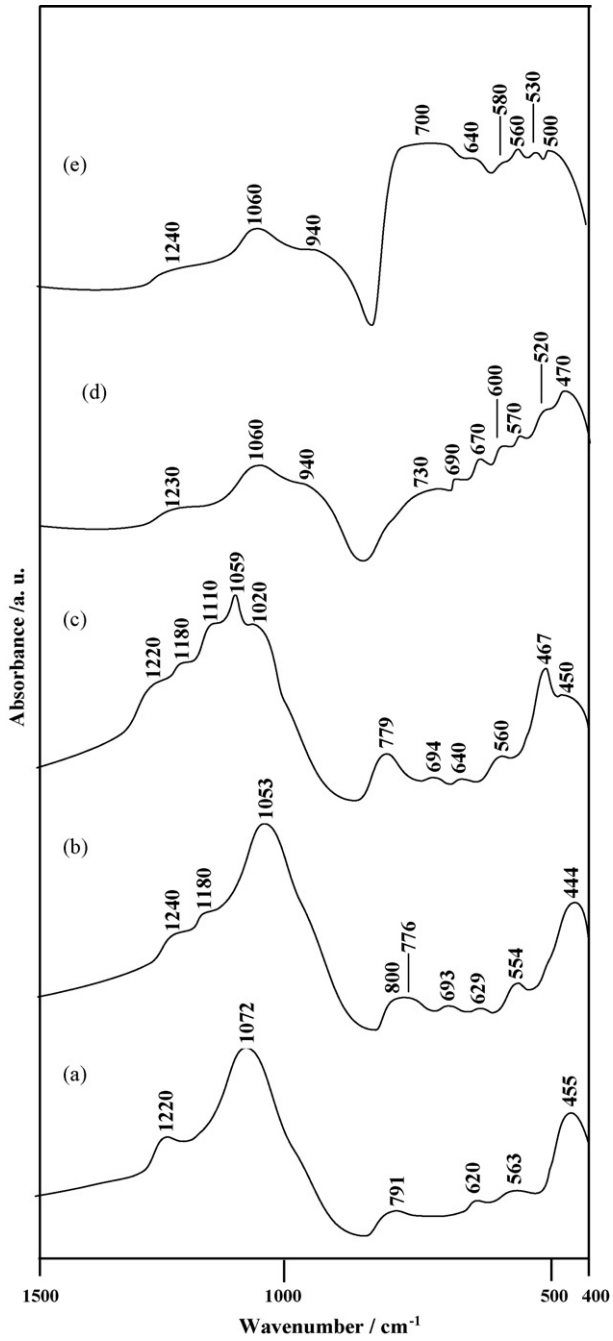

Fig. 3. FT-IR spectra of mordenite and Ti-mordenite samples prepared by different methods: (a) M; (b) TiM_{in}; (c) NH_4NO_3 treated TiM_{in}; (d) TiM_{imp}; and (e) TiM_{ss}.

tions of tetrahedral and framework atoms in mordenite zeolite [31]. The IR spectrum of TiM_{in} was similar to that of M except shifting the band at 1072 into 1053 cm^{-1}; advocating the well incorporation of titania, as well as appearing a band at 693 cm^{-1} and a shoulder at 1180 cm^{-1} those do not show up in the spectrum of M. Ti incorporation in the framework does not alter the wavenumber of the zeolite framework band at 563(554) cm^{-1} characteristics of secondary building unit, however, in post-synthesis methods (TiM_{ss} and TiM_{imp}) some changes in band intensity as well as its shape has been occurred in M structure presuming marked decrease in crystallinities of these samples, as elaborated previously from XRD investigations. In contrast to TiM_{in}, a band at 950(940) cm^{-1} due to vibration of Si–O–Ti linkages is observed in TiM_{ss} and TiM_{imp} [32]. Incorporation of titania within zeolite structure in the TiM_{in} sample is identified through splitting the 791 cm^{-1} band of νT–O into doublet at 776 and 800 cm^{-1}.

As a result of perturbation caused by Ti^{4+} in the stretching vibration of Si–O bonds, the TiM_{ss} and TiM_{imp} samples reveal some variations such as splitting of the 563(554) cm^{-1} band into 560 and 580 cm^{-1}, in TiM_{ss}, as well as 570 and 600 cm^{-1}, in TiM_{imp}, that ascribed to the high concentration of defect sites and crystallite strain along a specific crystallographic direction [33]. In addition, the band of Al–O belongs to alternating SiO_4 and AlO_4 tetrahedra at 620 cm^{-1} [33] is shifted to higher wavenumbers; into 640 cm^{-1} in TiM_{ss} and to 670 cm^{-1} in TiM_{imp}, presuming a dealumination process. The broadening of the bands at 640 and 670 cm^{-1}, which usually provoked from interfering amorphous Al (non-framework) species deposited as a result of dealumination with those of Al in the structure, confirm the latter assignment [34].

Obviously, IR spectroscopy gives direct information on the titanium species in zeolite; highly dispersed framework TiO_x stimulates the formation of the 940(950) cm^{-1} band in TiM_{ss} and TiM_{imp} samples in addition to extra-framework anatase TiO_2 that gives rise to bands at 520 and 730; in TiM_{imp}, and 500, 530 and 700; in TiM_{ss}. These bands were indeed shown in the IR result of an anatase TiO_2 sample (not shown) and; ascribed to Ti–O bonds and rather, emphasized by Gao et al. [33] during their studies on titanium silicalite-1 using FT-Raman spectroscopy. The recognized absence of the fingerprint band of $Si\cdots O^{\delta-}\cdots Ti^{\delta+}$ at 950(940) cm^{-1} in TiM_{in} is probably compensated by the shapely band at 1030 cm^{-1} that has been assigned by others to the same species [29,30]. For figuring out the presence of this band (1030 cm^{-1}), washing with NH_4NO_3 solution (1 M) was carried out. Hence bands at 1020 and 1110 cm^{-1} are exposed, as a result of decreasing sodium ions (Fig. 3c) [34]. This implies that the amount of titanium incorporated into the framework increases as the amount of Na^+ ions decreases. A band at 1125 cm^{-1} was identified by Zecchina and co-workers [35] during studying IR spectra of TS-1 and taken as a criterion for Ti–O–Si linkages. However, recognizing two bands in our case could be correlated to the varied environment around Ti atoms in the mordenite framework. The shoulder at 1180 cm^{-1} is intensified after exchanging with NH_4NO_3 and rather forms a distinct band. This band is unambiguously associated with a totally symmetric vibration of the TiO_4 tetrahedron, achieved through in-phase antisymmetric stretching of the four connected Ti–O–Si bridges [36].

3.5. UV–vis diffuse reflectance spectroscopy

Fig. 4 shows diffuse reflectance spectra in the UV–vis region for various Ti-mordenite samples, in comparison with that of M sample. The UV–vis spectrum of the parent sample reveals a band at 240 nm correlated with the zeolite structure [37]. The absorption band at about 200–260 nm are due to electron

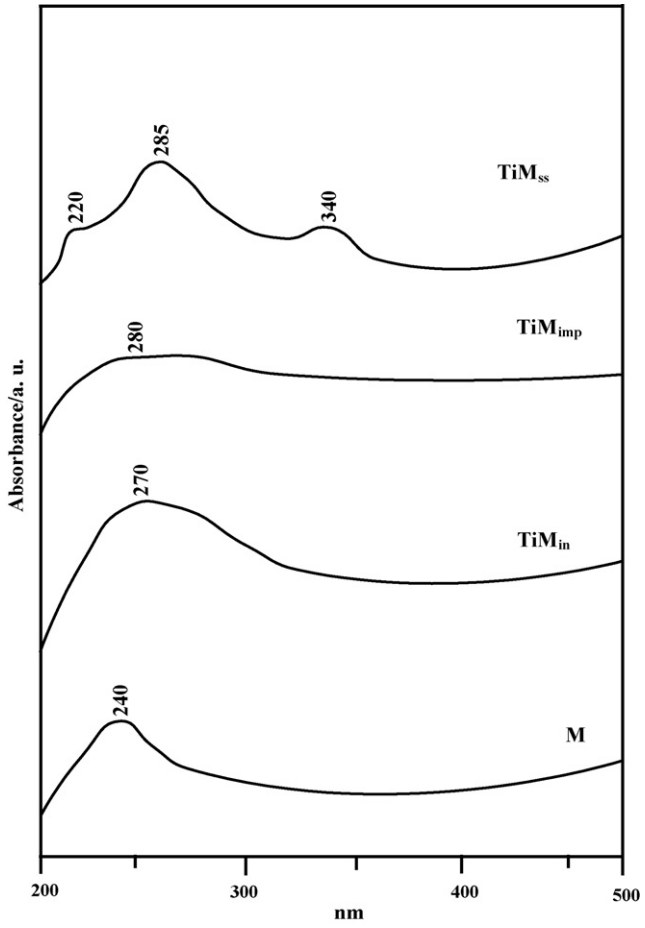

Fig. 4. UV–vis spectra of mordenite and titanium mordenites prepared by different methods.

excitation from ligand oxygen to an unoccupied orbital of the framework Ti^{4+}[38] in Ti-ligand samples and the maximum at 340 nm, that has been seen only in TiM_{ss}, are assigned to the absorption band of Ti^{4+} species in extraframework TiO_2 particles [39]. Concurrently, the TiM_{ss} sample exposed different Ti species of varying nature and coordination namely tetrahedral Ti^{4+} ions (220 nm; charge transfer from oxygen to tetrahedral Ti in zeolite framework), highly dispersed Ti species (285 nm) and anatase TiO_2 at 340 nm ($O^{2-} \rightarrow Ti^{4+}$). According to several studies, the broad peak of a maximum at 285 nm; in TiM_{ss} and at 280; in TiM_{imp}, can be attributed to the presence of site-isolated Ti atoms in penta-or octahedral coordination [40]. It can also be ascribed to Ti–O–Ti linkages in micro-domain of titania as exhibited previously during synthesis of amorphous TiO_2/SiO_2 that give absorption bands in the range of 260–320 nm [41]. Revealing TiO_2 anatase in XRD results of these samples support the presence of oligomeric TiO_2 species of higher crystallites size in TiM_{ss} (340 nm) than that in TiM_{imp}.

The presence of the broad band at 270 nm in TiM_{in} strongly suggest attributing the major part of Ti into tetrahedral Ti^{4+} sites, as emphasized from the absence of TiO_2 species in XRD results in addition to developing of some Ti^{4+} ions in tetrahedral coordination with silica forming Ti–O–Si linkages as devoted from IR outcomes.

3.6. Pyridine adsorption

Fig. 5 shows the FT-IR spectra of pyridine (Py) adsorption on various Ti-mordenite samples in comparison with that of M at 25 °C and following evacuation at 100 °C. The spectrum of Py/M at 25 °C exhibits a strong band at 1444 cm^{-1} due to Lewis pyridine (LPy) and a weak band at 1555 cm^{-1} due to Brönsted pyridine (Bpy). The display of the band at 1645 cm^{-1} is accounted for Bpy species bound probably to strong Bronsted acid sites, besides the ones at 1612 and 1632 cm^{-1}, those no doubt belong to Lewis acid sites. In this essence, one can attribute the small band at 1650 cm^{-1} to another Bpy species. Evacuation of the sample at 100 °C, indicates a decrease in intensity for the Lpy bands at 1612 and 1632 cm^{-1} in favor of Bpy at 1650 cm^{-1} with revealing no frequency shifts following the evacuation.

The spectrum exhibited by Py/TiM_{in} at 25 °C displays the same bands seen by M with an obvious increase in intensity of the Lpy band at 1442 cm^{-1}. In addition, bands at 1488, 1595, 1660, 1682 and 1694 cm^{-1} were also detected implying an oxidative breakdown of some Lpy into carboxylate species (band at 1595 cm^{-1}) [42]. On the other hand, the formation of α-pyridone species (νC=O band at 1682 cm^{-1}) reveals the existence of active nucleophlic (basic) OH groups on this sample [43]. Outgassing at 100 °C retained all the bands back with some variations including a decrease in intensity of Lpy (1442 cm^{-1}), an increase in intensity of Bpy (1539 cm^{-1}) as well as emerging of a new band at 1502 cm^{-1} characteristics of carbonaceous species [44,45].

For the TiM_{imp} sample, at 25 °C, a smaller amount of acid sites (1440 and 1545 cm^{-1}) than TiM_{in} was observed together with H-bonding Py bands at 1590 and 1475 cm^{-1} those show instability following outgassing at 100 °C. This sample also shows Lpy bands at 1620 and 1635, Bpy at 1655 as well as α-pyridone band characterized by C=O vibrations at 1685 cm^{-1}. Outgassing at 100 °C stimulates the formation of two different types of Brönsted acid sites (1550 and 1530 cm^{-1}) together with revealing an appreciable intensity for the 1490 cm^{-1} band implying the presence of appreciable acidic sites after evacuation at 100 °C. In concordance with the prevailage of Brönsted acidity, Lpy bands at 1620 and 1635, provoked at 25 °C, were vanished and showed instead a shoulder at 1625 cm^{-1}. This revealed decrease in Lewis acidity was in favor of that for Brönsted ones (1530, 1550 and 1645 cm^{-1}) following evacuation rather than that due to α-pyridone (oxidation products, 1680 cm^{-1}) that suffered a marked decrease. Indeed, this sample shows a higher appreciable Brönsted acidity as well as lower basic sites when compared with those on TiM_{in} sample.

For the TiM_{ss} sample, at 25 °C, no FTIR bands in 1539–1550 and 1442–1445 cm^{-1} regions, characteristic, respectively, to Brönsted and Lewis acid sites were observed. Only a band at 1490 cm^{-1} was present. This suggests the decrease in acidic sites of this sample. In addition, this sample shows H-bonded Py bands at 1436 and 1582 cm^{-1}. The latter bands were vanished following evacuation at 100 °C emphasizing their assignments. In the 1700–1600 cm^{-1} region bands due to Lpy; at 1608, 1632

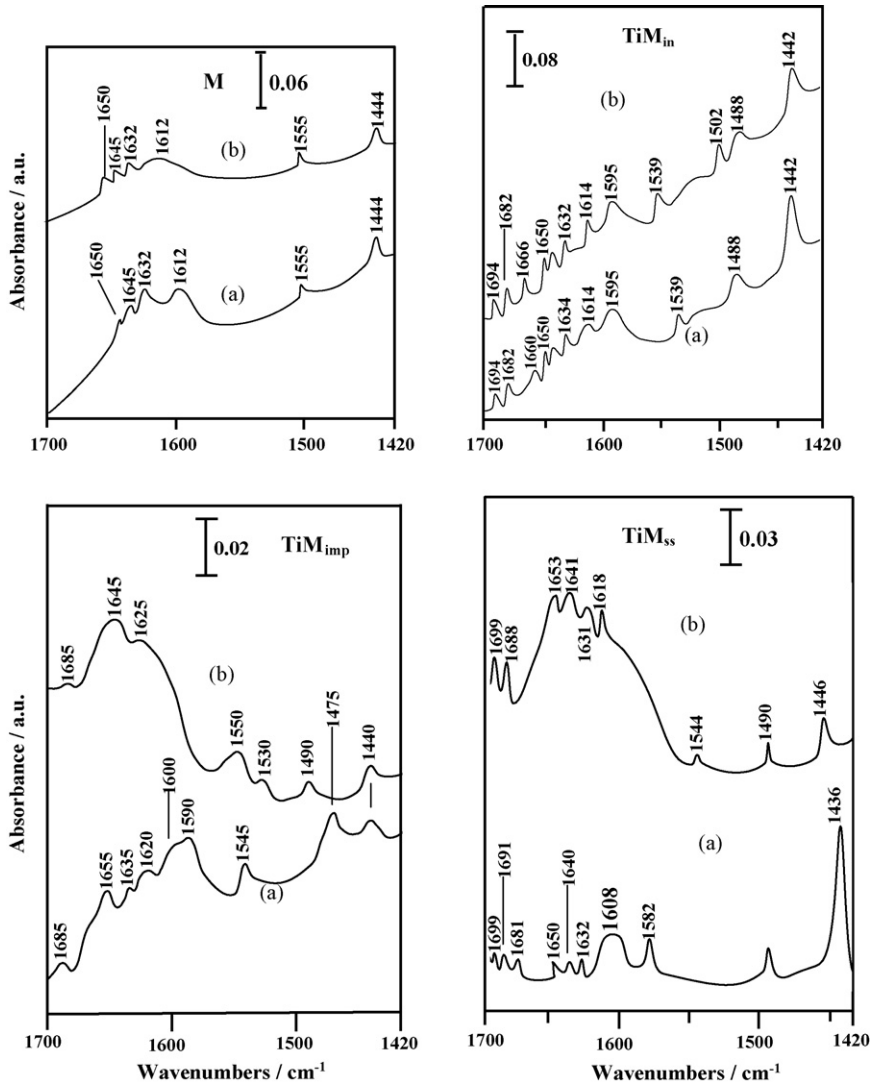

Fig. 5. In situ FT-IR spectra of pyridine adsorption on mordenite and Ti/mordenite prepared by different methods. Pyridine was introduced at room temperature and the spectra were recorded after evacuation for 15 min. (a) Evacuation at 25 °C and (b) evacuation at 100 °C.

and 1640 cm^{-1}, Bpy; at 1650 cm^{-1} and oxidative products of pyridine; at 1681, 1691 and 1699 cm^{-1}, were observed. Evacuation at 100 °C, stimulates the formation of Lpy band at 1446 and Bpy band at 1544 cm^{-1} as well as enhancing all the bands in the 1700–1600 cm^{-1} region confined for Lpy, Bpy and oxidative Py species. Following evacuation at 100 °C, a higher amount of Brönsted acid sites is depicted for this sample than TiM_{imp} and TiM_{in} ones to be in the order: $TiM_{ss} > TiM_{imp} > TiM_{in} > M$. On the other hand, the basic sites on TiM_{ss} were comparable to those on TiM_{in}. The concentration of Lpy in TiM_{ss} (1436 cm^{-1}) was found to be higher than those in TiM_{imp} and TiM_{in}. Accordingly, evacuation of Py at 100 °C for TiM_{ss} stimulates the formation of acid–base pair sites.

3.7. Activity test

3.7.1. Adsorption of meta-chlorophenol on various samples

Adsorption kinetics of *meta*-chlorophenol (MCP) on various catalysts were conducted in order to reveal whether or not the adsorption capacity, beside the other parameters that will be thoroughly investigated, affected the Photocatalytic activity. The adsorption isotherms of MCP on various catalysts, shown in Fig. 6 revealed the followings: (i) the adsorption rate of MCP on mordenite recorded the lower affinity comparatively revolving lower electron accepting capacity, i.e. low Lewis acidity; (ii) among Ti-mordenites, TiM_{in} and TiM_{ss} showed the highest adsorption capacity (25–27%). This is probably caused by complexation between the oxygen lone-pair electrons of phenol and newly developed Lewis acid sites (Ti^{+4}) on mordenite especially TiM_{in} that showed both strong and high density Lewis acid sites, as envisaged using Py adsorption. Indeed, cation exchangeable sites generated when Si is replaced by Ti framework [46] are primarily responsible for the adsorption of MCP; (iii) the order of the adsorption capacity of the samples is $TiM_{in} \approx TiM_{ss} > TiM_{imp} > M$. The adsorption isotherm (not shown) of MCP adsorption amount versus equilibrium concentration of aqueous MCP) on all TiM samples were measured at pH 6.5; which is close to the isoelectric point

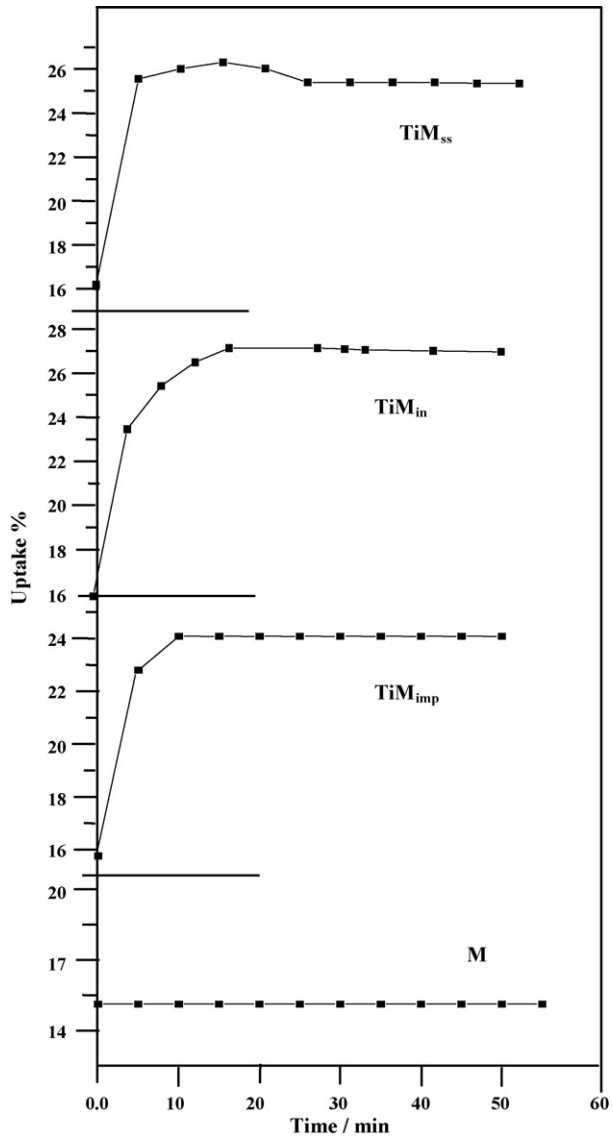

Fig. 6. Sorption kinetics of *m*-chlorophenol on M and TiM samples. Concentration at 5×10^{-3} and temperature 25 °C.

(IEP) of titania (~6.1), to nullify the electrostatic interaction between MCP and titania incorporated mordenites. They fit well with Langmuirian type isotherm and the calculated equilibrium constant K was found to be 0.15×10^3, 0.25×10^3, 0.3×10^3 m^3/mol for TiM$_{imp}$, TiM$_{ss}$ and TiM$_{in}$, respectively; (iv) the adsorption saturation was reached in a fewer time on TiM$_{imp}$ than that on TiM$_{in}$, i.e. forming a plateau, reflecting the facile reaching of MCP into the active sites of the former that showed the highest specific surface area, comparatively. This might indicate that the extent of adsorption is undeniably depend on the surface area of the adsorbent but more importantly depend on the surface polarity of the adsorbent as well as the diffusion of MCP (mass transfer). In this essence, the TiM$_{imp}$ sample presented the lowest pore radius (20 Å) between all TiM samples, hindering the transport of the adsorbate molecules when compared with TiM$_{ss}$, i.e. pore diffusion limitation.

3.7.2. Photocatalytic degradation of MCP

Fig. 7 presents the MCP photodegradation kinetics and permits a direct comparison of the performance of the titania modified catalysts. Under the experimental conditions used, the photocatalytic curves follow first-order reaction kinetics. It is well established [47–49] that photocatalysis experiments follow the Langmuir–Hinshelwood model, where the reaction rate R is proportional to the surface coverage θ,

$$R = -\frac{dC}{dt} = k_r\theta = \frac{k_r KC}{1 + KC}, \quad (2)$$

where k_r is the reaction rate constant, K the adsorption coefficient of the reactant, and C is the reactant concentration. When C is very small, the KC product is negligible with respect to unity so that Eq. (2) describes a first order kinetics. The integration of this equation with the limit condition that at the start of irradiation, $t = 0$, the concentration is the initial one,

$C = C_o$, gives

$$-\ln\left(\frac{C}{C_o}\right) = K't, \quad (3)$$

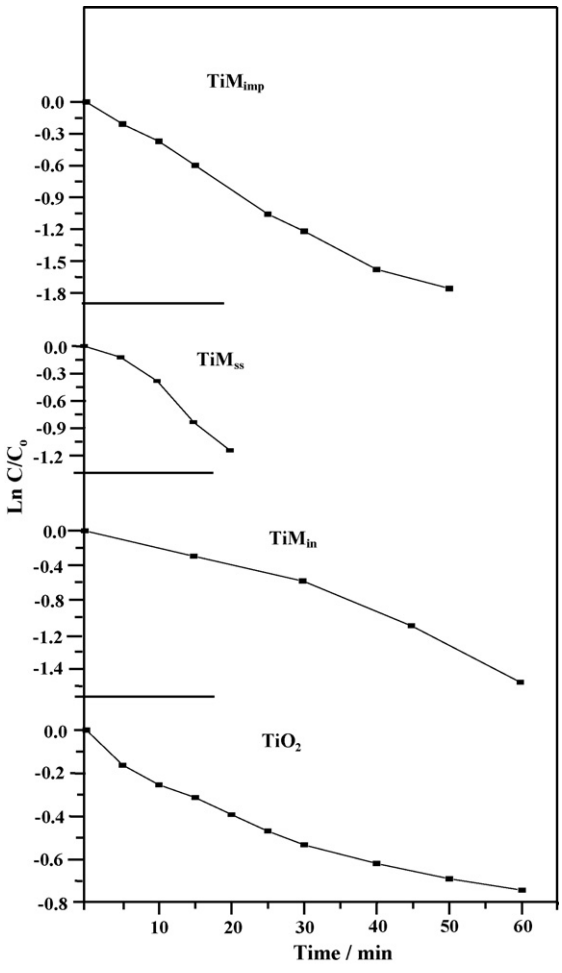

Fig. 7. $\ln C/C_o$ vs. time of Ti-mordenites catalysts in comparison with TiO_2-Degussa.

where K' is the apparent first-order reaction constant. The kinetic parameter K' resulting from the application of Eq. (3) indicates the following sequence; TiM_{ss} (0.060 min^{-1}) > TiM_{imp} (0.050 min^{-1}) > TiM_{in} (0.025 min^{-1}) > TiO_2 (P-25) (0.018 min^{-1}).

This figure illustrates that mordenites encapsulated TiO_2 photocatalysts require shorter irradiation time to complete mineralization than bare TiO_2 due to good adsorption of MCP anions and its intermediates on the zeolite surface where •OH radicals are available. The marked higher rate observed for TiM_{ss} (in only 20 min) could be due to the largest pore radius possessed by the catalyst (29 Å) in addition to higher amounts of well-crystallized nanoshaped extraframwork TiO_2 anatase (500, 530, 700 cm^{-1} as well as 340 nm band) that exceeded ones devoted from TiM_{imp}. The shape of TiM curves (except TiM_{ss}) seems hindered as time elapsed, i.e. the extent of degradation is slowed down, probably due to formation of intermediates and their competitiveness with MCP anions in the photocatalytic degradation process. The difference of the MCP removal between the UV-illuminated and dark (adsorption) conditions (Δ [UV-dark]) can be used as an apparent measure to evaluate the impact of the UV-illumination on the MCP degradation. TiM_{ss} gives a value equal to 74% ([100 − 26]) in a degradation profile extends only to 20 min reflecting an increase in the density of long lived •OH radicals comparatively. The possibility of leaching some titanium dioxide from mordenite structure was indeed followed by AAS technique and thus values comprised of 0.05–0.1 ppm were revealed. The loss of titanium into the solution of the mixture could be caused by the formation of hydroperoxo–titanium complex [50]. The amount of leached TiO_2 from TiM_{ss} was the highest (0.1 ppm) between all catalysts. The TiM_{in} catalyst did not show any TiO_2 amounts at the end of the reaction suggesting that most of titanium is associated within the zeolite framework. Heterogeneous reactions rather than homogeneous ones are devoted principally on these photocatalysts.

From these results, a highly efficient photocatalytic oxidation of MCP can be achieved using the TiM_{ss} catalyst, which includes highly dispersed anatase TiO_2 as active species, while dispersed Ti–O where the Ti^{4+} was tetrahedrally coordinated are less candidate for MCP oxidations. These results indicate the ability of mordenites in favoring photo-induced electron-transfer reactions and retarding back electron transfer ones [51], i.e. zeolite support delocalizes photo-generated electrons thus prohibiting and/or delaying its recombination with holes.

Cl^- was released upon degradation of MCP in all tested catalysts and this process was shown to be very fast while using the TiM_{ss} catalyst that showed the highest degradation rate although of the fear of readsorbing Cl^- on the catalyst surface and thus slowing the rate of formation of reactive •OH. At the time of complete disappearance of MCP (within 60 min in the TiM_{in} catalyst (Fig. 8) about 90% of stoichiometric amount of Cl^- was recovered suggesting that Cl^- containing intermediate compounds are produced in the mineralization process. However, the pH of all mixtures changes from 6.27 to 2.5–2.0 at the end of the reaction. Quite amounts of Cl^- react on the other hand, to form HCl, which influences the surface state of titanium containing mordenites and the ionization state of the ionizable MCP molecules. For pH's lower than PZC of titania (6.1), [52] the surface become positively charged and the following equilibrium can be expected:

$$Ti{-}OH + H^+ \leftrightarrow TiOH_2{}^+ \quad (4)$$

Since MCP has a negatively charged phenolate function (O^-), its adsorption is favored on a positively charged surface. This result indicates that the acidic solution favors the adsorption of MCP onto the photocatalyst surface. However, the devoted variation in the kinetics of MCP disappearance on various catalysts could be correlated with the extent of Cl^- released to intervene with protons to form HCl in short time thus, making the mixture more acidic to further share in enhancing the rate of reaction. In addition, zeolites are known to stabilize reactive intermediate in several photochemical reactions [53] and the reactivity of short chain aliphatic compounds with •OH radicals is usually slow. These difficulties have been overcome in TiM_{ss} due to the facile mobility of MCP molecules onto the photoactive TiO_2 sites present on mordenites surfaces capable of forming reactive •OH radicals. On the other hand, crystallites size of TiO_2 on M in TiM_{ss} is small enough to prohibit scattering of UV light thereby, an electron transfer from excited state of MCP to TiO_2 on M (in TiM_{ss}) is generated [54].

Following up the decay of MCP by HPLC for all TiM catalysts indicated the same products assuming a similar mechanism. Thus, as an example, the product distribution of the TiM_{ss} catalyst is examined in details (Fig. 8). The primary

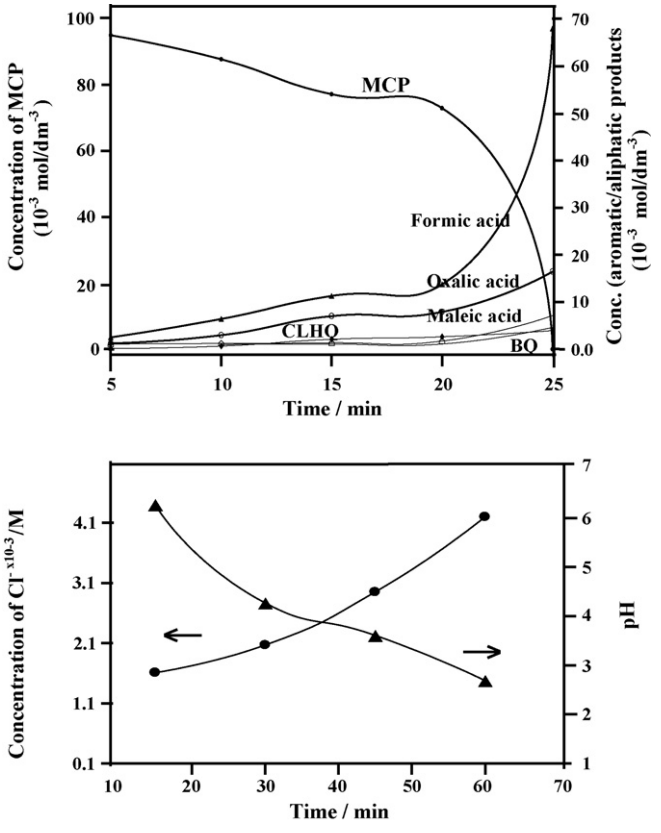

Fig. 8. Photocatalytic degradation of *m*-chlorophenol and formation of Cl^- and intermediates on the TiM_{ss} catalyst (0.10 g) as deduced by HPLC and ion chromatography Techniques.

aromatic intermediates identified by HPLC were chlorohydroquinone (CLHQ) and benzoquinone (BQ). Besides, some aliphatic compounds (carboxylic acid and specifically maleic, oxalic and formic acids) were also identified. Since the former products exhibit high UV absorption, their low peak area does not allow their unambiguous identification, however, the latter products, specifically formic acid, appears appreciably at the end of the irradiation time. Thus, the lack of aromatic compounds to be present in significant amount suggests a reasonable efficient ring-opening reaction under the conditions applied. On the basis of our results and literatures devoted for photocatalytic decompositions of *ortho* and *para* chlorophenoles [55,56] the following (simplified) mechanism is proposed for the photocatalytic degradation of MCP (Fig. 9). The initial degradation step; following the photochemical generation of •OH radicals, is the attack on aromatic ring to yield substituted chlorodihydroxycyclo-hexadienyl radical (1) [57]. Some authors consider that H abstraction may also play an important role (2), and direct electron abstraction from the aromatic compound by •OH to give resonance-stabilized cations radical is also presumed to be of importance [58]. •OH addition in the *para* position to 3-chloro-phenol, followed by H-abstraction leads to chlorohydroquinone (3). This suggests that a highly favored addition of •OH in the *para*-position is formed nullifying those might take place in *ortho* positions due to steric factors. The process is then initiated to form *p*-benzoquinone (4) by realsing either Cl^- (dechlorinations) or HCl formation, as has been confirmed previously. One cannot deny that ring cleavage could be responsible for chlorohydroquinone-benzoquinone transformation. Further, degradation of *p*-benzoquinone with •OH and/or O_2 leads to maleic acid (5) that can be mineralized to CO_2 via either oxalic (6) or formic acids (7) those indeed strongly accelerated by •OH radicals.

To have a clue about the adsorbed species onto the catalyst surface after MCP degradation on TiM_{ss}, an FTIR spectrum was undertaken for the sample following the reaction as illustrated in Fig. 10, in comparison with that of TiM_{ss}, not exposed to the reaction. As it can be seen, oxidized fragments of COO groups can easily be identified by the characteristic absorption bands in ν_s(1330–1480 cm^{-1}) and ν_{as}(1500–1620 cm^{-1})

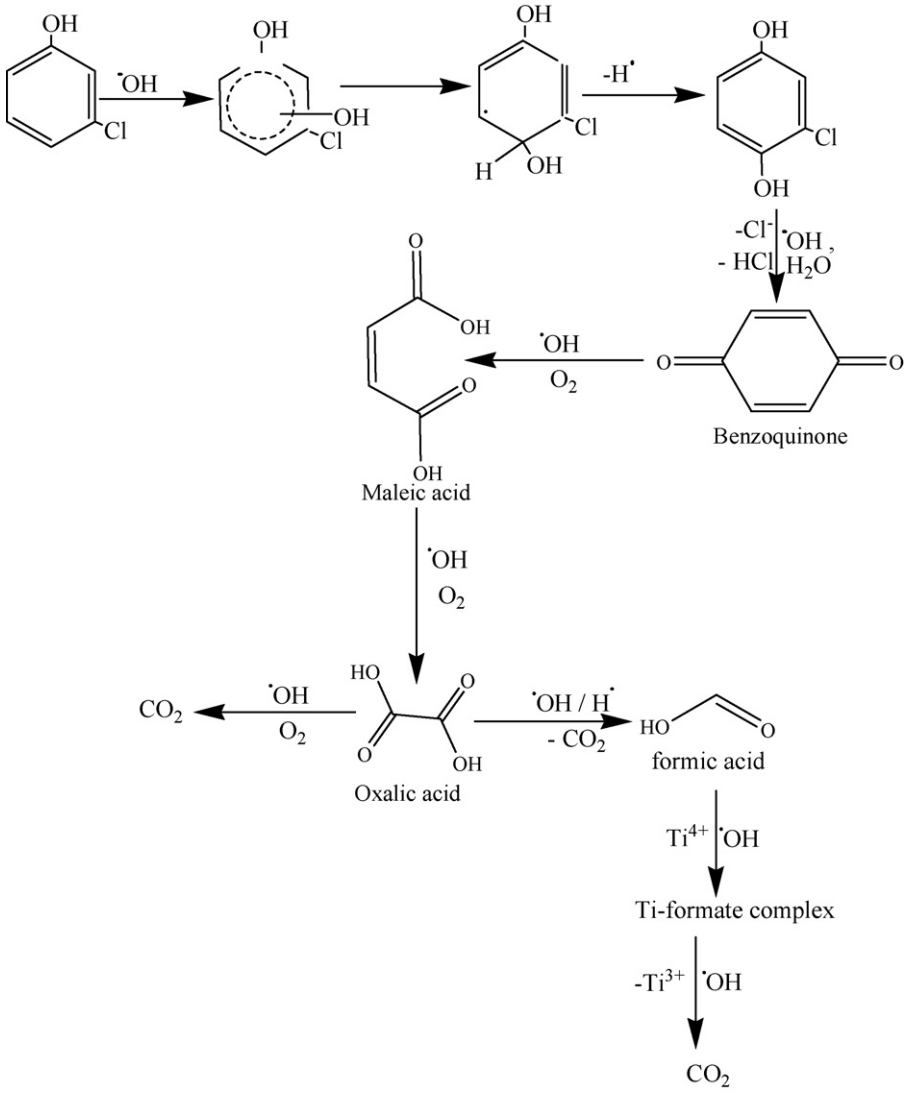

Fig. 9. General reaction pathway proposed for *meta*-chlorophenol minerlization as catalyzed by TiM_{ss} under UV irradiation.

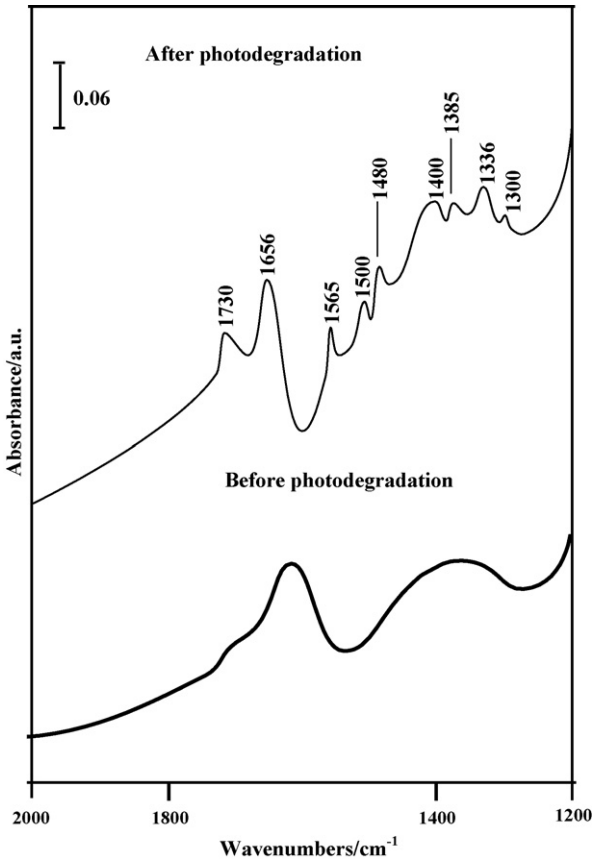

Fig. 10. FT-IR spectra of TiM_{ss} befor and after photodegradation of *meta*-chlorophenole.

regions [59]. This indicates the presence of both formate ($\nu_{as}HCOO^-$: 1565 cm^{-1}; ν_sHCOO^-: 1336 cm^{-1}) and carboxylate (1400–1480 cm^{-1}) groups. Furthermore, formic acid vibrational band at 1730 cm^{-1} characteristics of $\nu C{=}O$ was also seen together with a small band at 1385 cm^{-1} due to the $\delta(C{-}H)$ vibration. Similar bands at $\nu_{as}(HCOO^-$: 1600–1560 cm^{-1}), $\nu_a(HCOO^-$: 1370–1306 cm^{-1}) and 1730($\nu C{=}O$) were depicted when formic acid adsorbed on TiO_2 and they are assigned to formate and formic acid species, respectively. The presence of C–H stretching vibration bands at 2840 and 2930 cm^{-1} (not shown) emphasize the formation of formate species and in the same time nullifies the possibility of founding any aromatic intermediates due to the absence of C–H stretching band of aromatic moieties over 3000 cm^{-1}. It can be noted that formic acid and/or formate molecules were the last degraded organic molecules detected before mineralization and found in major amounts than those of oxalic acids. Thus, one might assign the bands occurred in the 1480–1400 cm^{-1} range to other oxalate or to adsorbed formate on Ti atoms and/or Na-mordenite.

No significant changes concerning mordenite framework (560 cm^{-1}) were revealed, following the photocatalaytic decomposition together with the persistence of the band at 968 cm^{-1}, ascribed to Ti–O–Si linkages evidencing the stability and integrity of the structure and probably to the non-significant role of latter moieties.

4. Conclusions

The Photocatalytic degradation of *meta*-chlorophenol (MCP) that has been performed by Ti-mordenites in conjunction with UV irradiation was examined. The investigated performance of the catalysts for MCP degradation was directly correlated with their structural and acidic characterizations, which have been thoroughly investigated using XRD, thermal analysis, N_2 adsorption, FT-IR, UV–vis and pyridine-FTIR techniques. The results were as follows:

1. The TiM_{ss} catalyst exhibited the highest rate of degradation exceeding rest of the samples. This was due to the offered large pore radius (29 Å) and anatase TiO_2 species (500, 530 and 700 cm^{-1} and 340 nm). Si–O–Ti linkages were observed in TiM_{ss} [950(940 cm^{-1})] and showed no significant role in the reaction besides, high concentrations of defect sites and crystalline strain as a result of TiO_2 insertion. The dechlorinations of Cl^- as HCl increased up the reaction rate tremendously due to decreasing the pH to be lower than the ZPC of TiM_{ss} (from 6.27 to 2.0) thus favoring the adsorption of MCP, which acquired negatively charged phenolate groups. The acidity of TiO_2 encapsulated inside mordenites helps in accelerating the activity compared with bare TiO_2 due to improved adsorption of MCP (increasing number of Lewis sites) and delocalization of photogenerated e^-/h^+ by zeolite substrate.
2. Only aliphatic compounds were revealed on final stages of degradation most importantly formates (formic acid) that represented major part of these compounds. TiM_{ss} never showed any changes in structure after performing the reaction reflecting the stability of the catalyst, that indeed needs further investigation to clarify the extent of its stability for industrial application.
3. Incorporating titania inside the framework of zeolite minimizes the photoeffciency of dispersed Ti–O (where Ti^{4+} is in tetrahedral structure) as seen in TiM_{in}. Similarly, the strong interaction between TiO_2 and zeolite also affects the photoeffciency of TiO_2 as seen in TiM_{imp}. The decreased pore radius, in this sample, hinders the mobility of MCP to the photocatalytic TiO_2 sites.

References

[1] J.E. Gilbert, A. Mosset, Mater. Res. Bull. 33 (1998) 997.
[2] P.K. Bajpai, Zeolites 6 (1986) 2.
[3] G.A. Ozin, A. Kuperman, A. Stein, Angew. Chem. Int. Ed. Eng. 28 (1989) 259.
[4] D. Cox, T.E. Gier, G.D. Stucky, J. Birlein, J. Am. Chem. Soc. 110 (1988) 2986.
[5] Y. San, T. Song, S. Qlu, W. Pang, J. Shen, D. Jiang, Y. Yue, Zeolites 15 (1995) 547.
[6] J. Warzwoda, A.G. Dixon, R.W. Thompson, A. Sacco, j.S.L. Suib, Zeolites 16 (1996) 125.
[7] S. Qiu, J. Yu, G. Zhu, O. Terasaki, Y. Nozue, W. pang, R. Xu, Microporous Mesoporous Mater. 21 (1998) 245.
[8] C. Shao, X. Li, S. Qiu, F. Xiao, O. Terasaki, Microporous Mesoporous Mater. 39 (2000) 117.
[9] M.M. Mohamed, J. Colloid Inter. Sci. 265 (2003) 106.

[10] T.M. Salama, M.M. Mohamed, I. Othman, G.A. El-shobaky, Appl. Catal. A 286 (2005) 85.
[11] M.M. Mohamed, T.M. Salama, I. Othman, I. Abdallah, Microporous Mesoporous Mater. 84 (2005) 84.
[12] R. Millini, E.P. Massara, G. Perego, G. Bellussi, J. Catal. 137 (1992) 497.
[13] A. Thangaraj, R. Kumar, S.P. Mirajkar, P. Ratnasamy, J. Catal. 130 (1991) 1.
[14] G. Deo, A.M. Turek, I.E. Wachs, D.R.C. Huybrechts, P.A. Jascobs, Zeolites 13 (1993) 365.
[15] E. Astorino, J.B. Peri, R.J. Willey, G. Busca, J. Catal. 157 (1995) 482.
[16] S.O. YaO-Matsuo, M. Ueda, J. Photochem. Photobiol. A 168 (2004) 1.
[17] O. Legrini, E. Oliveros, A. Braun, Chem. Rev. 93 (1993) 671.
[18] J. Matos, J. Laine, J.M. Herrmann, Appl. Catal. B 18 (1998) 291.
[19] N. Takeda, T. Torimoto, S. Sampath, S. Kuwabata, H. Yoneyama, J. Phys. Chem. 99 (1995) 986.
[20] H. Uchida, S. Itoh, H. Yoneyama, Chem. Lett. (1993) 1995.
[21] N. Takeda, N. Iwata, T. Torimoto, H. Yoneyama, J. Catal. 177 (1998) 240.
[22] T. Ibusuki, K. Takeuchi, J. Mol. Catal. 88 (1994) 93.
[23] M.M. Mohamed, T.M. Salama, T. Yanaguchi, Colloids Surf. A 207 (2002) 25.
[24] P.G. Smirniotis, L. Davydov, Catal. Rev. Sci. Eng. 41 (1999) 43.
[25] W.S. Ju, M. Matsuoka, M. Anpo, Catal. Lett. 71 (2001) 91.
[26] M. Anpo, H. Yamashita, Y. Ichihashi, Y. Fujii, M. Honda, J. Phys. Chem. B 101 (1997) 2632;
M.M. Mohamed, M.M. Al-Esaimi, J. Mol. Catal. A 255 (2006) 53;
M. Matsuoka, M. Anpo, J. Photochem. Photobiol. C 3 (2003) 225.
[27] R. Bolton, S.R. Cater, in: R.G. Zepp, G.R. Helz, D.G. Crosby (Eds.), Aquatic and Surface Photochemistry, Lewis Publishers, Boca Raton, FL, 1994, p. 467.
[28] T. Sreethawong, Y. Suzuki, S. Yoshikawa, Int. J. Hydrogen Energy 30 (10) (2005) 1053.
[29] T. Ohno, Z. Miyamoto, K. Nishijima, H. Kanemitsu, F. Xueyuan, Appl. Catal. A 302 (2006) 62.
[30] A.M. Velarde, P. Bartl, T.E.W. Nieben, W.F. Holederich, J. Mol. Catal. A 147 (2000) 225.
[31] A. Carati, C. Flego, E. Previde Massara, R. Millini, L. Carluccio, W.O. Parker Jr., G. Bellussi, Microporous Mesoporous Mater. 30 (1999) 137.
[32] A. Trovarelli, G. Dolcetti, C. de Leitenburg, J. Kaspar, P. Finetti, A. Santoni, J. Chem. Soc. Faraday Trans. 88 (1992) 1311.
[33] H. Gao, W. Lu, Q. Chen, Miroporous Mesoporous Mater. 34 (2000) 307.
[34] H. Okaniwa, M. Kasagen, Japan Patent 2, 149 (1990) 416.
[35] G. Ricchiardi, A. Damin, S. Bordiga, C. Lamberti, G. Spano, F. Rivetti, A. Zecchina, J. Am. Chem. Soc. 121 (2001) 11409.
[36] S. Bordiga, A. Damin, G. Berlier, F. Bonino, G. Ricchiardi, A. Zecchina, C. Lamberti, Int. J. Mol. Sci. 2 (2001) 167.
[37] M.M. Mohamed, I. Othman, N. Eissa, Appl. Catal. A 87 (2005) 93.
[38] R.J. Dovis, Z. Liu, T.E. Tabora, W.S. Wielband, Catal. Lett. 101 (1995) 34.
[39] D. Ton, S.V. Nguyen, V. Hulea, E. Dunitriu, S. Kaliaguine, Microporous Mesoporous Mater. 57 (2003) 169.
[40] B. Notari, Stud. Surf. Sci. Catal. 37 (1988) 413.
[41] J. Klass, K. Kulawik, G. Schulz-Ekloff, Stud. Surf. Sci. Catal. 84 (1994) 2261.
[42] M.I. Zaki, G.A.M. Hussein, S.A.A. Mansour, H.A. El Ammawy, J. Mol. Catal. 51 (1989) 209.
[43] M.M. Mohamed, J. Mol. Catal. 200 (2003) 301.
[44] S. Huber, H. Knözinger, Appl. Catal. A 181 (1999) 239.
[45] M.M. Mohamed, Appl. Catal. A 367 (2004) 135.
[46] I. Moriguchi, M. Honda, T. Ohkubo, Y. Mawatari, Y. Teraoka, Catal. Today 90 (2004) 297.
[47] J.M. Hermann, Catal. Today 24 (1995) 157–164.
[48] N.T. Durg, N.V. Khoa, J.-M. Herrmann, Inter. J. Photoenergy 7 (2005) 11.
[49] P. Pichat, in: G. Ert, H. Knozinger, J. Weit Kamp (Eds.), Hand Book of Heterogenous Photocatalysis, VCH-Wiley, Weihein, 1997, p. P-2111.
[50] J. Grzechulska, A.W. Morawski, Appl. Catal. B 36 (2002) 45.
[51] M.V. Shanker, S. Anandan, N. Venkatachalam, B. Arabindoo, V. Murueesan, Chemosphere 63 (2006) 1014.
[52] I. Ilisz, A. Donbi, K. Mogyorosi, A. Forkas, I. Dekany, Appl. Catal. B 39 (2002) 247.
[53] R. Chatti, S.S. Rayalu, N. Dubey, N. Labhsetwar, S. Devotta, Solar Eng. Mater. Solar Cell 91 (2007) 180.
[54] J.J. Lee, Y. Kim, M. Yoon, J. Photosci. 8 (2001) 257.
[55] R. Sauleda, E. Brillas, Appl. Catal. B 29 (2001) 135.
[56] L. Jakob, T.L. Hashem, S. Burki, N.M. Guindz, A.M. Braun, J. Photochem. Photobiol. Chem. A 75 (1993) 97.
[57] M.E. Snook, G.A. Hamilton, J. Am. Chem. Soc. 96 (1974) 860.
[58] A.A. Davydov, Infrared Spectroscopy of Adsorbed Species on the Surface of Transition Metal Oxides, John Wiley & Sons, 1990, p. 148.
[59] J. Arana, O.G. Diaz, M.M. Saracho, J.M. Dona Rodriguez, J.A. Herrera Melian, J.P. Pena, Appl. Catal. B 32 (2001) 49.